Antagonist elastic interactions tuning spin crossover and LIESST behaviours in Fe II trinuclearbased one-dimensional chains

Narsimhulu Pittala, Emmelyne Cuza, Dawid Pinkowicz, Michal Magott, Mathieu Marchivie, Kamel Boukheddaden, Smail Triki

RESEARCH ARTICLE

Antagonist elastic interactions tuning spin crossover and LIESST behaviours in Fe^{II} trinuclear-based one-dimensional chains†

Narsimhulu Pittala,[a] Emmelyne Cuza,[a] Dawid Pinkowicz,[b] Michał Magott,[b] Mathieu Marchivie,[c] Kamel Boukheddaden[d] and Smail Triki*[a]

A new 1D coordination polymer, $[Fe_3(\mu_2\text{-bntrz})_6(bntrz)_2(\mu_2\text{-tcnsme})_2](tcnsme)_4{\cdot}4H_2O$ (**1·4H$_2$O**), based on $[Fe_3(\mu_2\text{-bntrz})_6]$ trinuclear units covalently linked by symmetric double cyanocarbanion coligands involving 12-membered metallacycles has been prepared and characterised. The crystal structure of **1·4H$_2$O** revealed a trinuclear fragment, $[Fe_3(\mu_2\text{-bntrz})_6(bntrz)_2(\mu_2\text{-tcnsme})_2]^{4+}$, composed of a central Fe^{II} ion (Fe1) and two external metal ions (Fe2), similar to that described for the discrete trinuclear complex $[Fe_3(\mu_2\text{-bntrz})_6(tcnset)_6]$ (**2**) previously reported. Magnetic studies of **1·4H$_2$O** showed a continuous gradual decrease of the magnetic signal, characteristic of the presence of a complete one-step gradual HS to LS transition ($T_{1/2}$ = 281 K) different from the abrupt one described for **2**. This difference has been attributed to the presence of competing ferro- and anti-ferroelastic interactions, induced, respectively, by the intra-(μ_2-bntrz) and inter-trimer (μ_2-tcnsme) covalent links in **1·4H$_2$O**. TGA and powder X-ray diffraction analyses revealed that **1·4H$_2$O** shows a complete and reversible "dehydration (**1**)/hydration (**1·4H$_2$O**)" process that occurs, respectively, by heating **1·4H$_2$O** at 370 K and by soaking in water the dehydrated sample (**1**). The magnetic behaviour of **1** exhibits a two-step SCO transition at *ca.* 245 K. Thanks to the combined magnetic and vibrational infrared data allowing correct extraction of the contribution of the two Fe^{II} active centres (one central Fe1 and two external Fe2 ions), the first step (370–245 K) was attributed to a concomitant HS/LS switching of the central Fe1 and a half of the Fe2 ions and the second one, occurring below 245 K, was attributed to the HS/LS transition of the remaining HS state among the randomly distributed Fe2 external ions. Photomagnetic experiments have been performed for both hydrated (**1·4H$_2$O**) and dehydrated (**1**) phases. As expected from their thermal transition temperatures, no photomagnetic response was observed for **1·4H$_2$O** at 638 nm nor at 450 nm, while the dehydrated phase (**1**) shows an increase of the magnetic moment, reaching a maximum of 1.4 cm^3 K mol^{-1} at 22 K, followed by the thermally-induced HS to LS relaxation with T_{LIESST} = 41 K.

Received 00th July 20XX
Accepted 00th July 20XX

DOI: 10.1039/XXXXXXXXXX

Introduction

Spin crossover (SCO) materials are likely among the most studied switchable molecular systems, because of their suitability to be integrated in electronic or spintronic devices.[1–14] In general, this phenomenon occurs in the first row transition metal complexes of d^4–d^7 electronic configurations for which the spin pairing energy is close to the ligand field strength, giving rise to strong changes in their magnetic, optical and structural chacateristics.[14] However, molecular systems based on Fe^{II} of d^6 electronic configuration, exhibiting a diamagnetic–paramagnetic transition from the low spin (LS) state (S = 0, $^1A_{1g}$) to the high spin (HS) state (S = 2, $^5T_{2g}$), are the most studied systems.[14–18] Among the few molecular systems exhibiting outstanding SCO behaviours, such as strong cooperativity around room temperature, those based on the rigid and potentially bridging triazole ligands are identified as the most attractive materials for potential applications in molecular electronics.[1–3,9–11] The latter include in particular the 1D coordination polymers $[Fe(Htrz)_2(trz)](X)$ and $[Fe((R\text{-}trz)_3](X)_2$ (Htrz = 4-H-1,2,4-triazole, R = functional group, X^- = regular or uncommon anions), exhibiting wide thermal hysteresis loops

aUniv Brest, CNRS, CEMCA, 6 Avenue Victor Le Gorgeu, C.S. 93837, 29238 Brest Cedex 3, France. E-mail: Smail.Triki@univ-brest.fr; Fax: +33 298016146
bFaculty of Chemistry, Jagiellonian University, Gronostajowa 2, 30-387 Kraków, Poland
cUniv. Bordeaux, CNRS, Bordeaux INP, ICMCB, UMR 5026, F-33600 Pessac, France
dUniversité Paris-Saclay, Université de Versailles Saint Quentin, CNRS, GEMaC UMR 8635, 45 Av. des Etats-Unis, 78035 Versailles Cedex, France

† Electronic supplementary information (ESI) available: Experimental pro-cedures, spectroscopic data for new compounds, and NMR and IR spectra (syn-thesis details and Fig. S1–S24). CCDC 2078819 (150 K) and 2078820 (298 K). For ESI and crystallographic data in CIF or other electronic format see https://dx.doi.org/10.1039/XXXXXXXXXX

around room temperature but for which accurate structural data are very scarcely reported.[19,20] Besides these 1-D systems, di- and trinuclear discrete complexes based on similar triple triazole bridges have also been reported, and most of them have been structurally characterised.[21–41] These polynuclear systems could help modeling and tuning the SCO characteristics of 1D coordination polymers, especially trinuclear complexes in which the central metal ion shows a similar environment to the one involved in 1D coordination polymers. Dinuclear systems show various SCO behaviours including abrupt or incomplete gradual thermal transitions and photo-induced LIESST effects,[21–27] and some of them stand out due to their multifunctional characteristics such as the presence of synergic SCO/fluorescence[21] or the on/off photo-control of magnetic interactions.[23] In contrast, in the major part of trinuclear systems, only the central Fe^{II} ion undergoes a SCO transition from the HS–HS–HS to HS–LS–HS states, while the two external metal ions remain in the HS state due to their FeN_3O_3 coordination environments involving water molecules or other oxygenated species acting as terminal ligands.[28–41] It is of interest to note, however, that all the trinuclear complexes based on neutral triazole triple bridges show poorly cooperative and incomplete transitions,[28–38] while one of the few anionic complexes based on sulfonated triazole ligands[39–41] show a thermal HS–HS–HS to HS–LS–HS transition above room temperature with an unexpectedly large hysteresis loop (>85 K) and the highest temperature at which the memory effect remains in a thermally quenched SCO system (T_{TIESST} = 250 K).[39]

Thus, to achieve true SCO trinuclear complexes with three active metal centres in which the central one displays a similar environment to those involved in 1D chain polymers and to favour the occurrence of cooperative effects along the linear trinuclear system, we have extended the above synthetic approach to the use of uncommon and sophisticated cyanocarbanions which can act as terminal or bridging coligands through their various N-donor nitrile groups.[42–46] This original approach led us recently to the SCO complex $[Fe_3(\mu_2\text{-bntrz})_6(tcnset)_6]$ (Scheme 1),[47] the first trinuclear complex based on triple triazole bridges exhibiting a [HS–HS–HS] ↔ [LS–LS–LS] one-step first-order spin transition above room temperature ($T_{1/2}$ = 318 K).

Although the two Fe^{II} centres (two external and one central metal ion) display two different FeN_6 environments, the overall transition takes place concomitantly due to the strong ferroelastic interactions along the trinuclear system. Besides its notable SCO characteristics, this trinuclear system constitutes an excellent object for theoretical investigations based on elastic models including competing interactions. In addition, this remarkable trinuclear complex was found to show very recently giant and reversible barocaloric effects.[48] In this context, and with the objective to understand the effect of the concomitant covalent and non-covalent elastic interactions on the cooperativity and on the occurrence of a one- or multi-step transition in this unique trinuclear unit, we report here a detailed study related to the new 1D coordination polymer $[Fe_3(\mu_2\text{-bntrz})_6(bntrz)_2(\mu_2\text{-tcnsme})_2](tcnsme)_4{\cdot}4H_2O$ (**1·4H$_2$O**) (Scheme 1), based on the $[Fe_3(\mu_2\text{-bntrz})_6]$ trinuclear units covalently linked through double cyanocarbanion coligands. Moreover, considering the similar trinuclear unit constituting this 1D chain (**1·4H$_2$O**) and the discrete complex $[Fe_3(\mu_2\text{-bntrz})_6(tcnset)_6]$ (**2**),[47] their different magnetic behaviours can be attributed to their slight structural differences to better understand the crucial role of the competing ferroelastic and anti-ferroelastic interactions on their SCO characteristics.

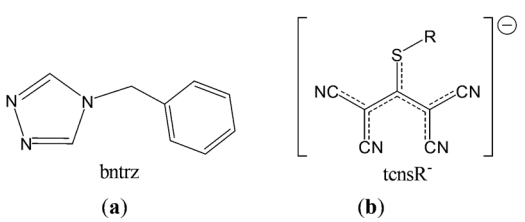

Scheme 1 (a) Structure of 4-(benzyl)-1,2,4-triazole (bntrz); (b) 1,1,3,3-tetracyano-2-thiomalkylpropenide cyanocarbanions ($tcnsR^-$): $tcnsme^-$ (R = CH_3), $tcnset^-$ (R = CH_2-CH_3).

Results and discussion

Ligand syntheses

The functionalized triazole ligand 4-(benzyl)-1,2,4-triazole (bntrz) was prepared by modifying a previously reported method (see details in the ESI and Fig. S1–S6†).[20,49] The potassium salt of the coligand 1,1,3,3-tetracyano-2-thiomethylpropenide [K(tcnsme)] was prepared in two steps according to the protocol previously described by some of us (see Fig. S7–S12†).[47]

Synthesis of $[Fe_3(\mu_2\text{-bntrz})_6(bntrz)_2(\mu_2\text{-tcnsme})_2](tcnsme)_4{\cdot}4H_2O$ (1·4H$_2$O)

Single crystals of complex **1·4H$_2$O** have been synthesized using the diffusion technique in a fine glass tube (5.0 mm diameter) by carefully layering an aqueous solution of the bntrz ligand onto a water–acetone solution containing both K(tcnsme) and $Fe(BF_4)_2{\cdot}6H_2O$ salts. The coordination polymer of **1·4H$_2$O** has been obtained within two weeks as micrometric needle shaped yellow single crystals at the interface of the solutions (see details in the ESI and Fig. S13†).

Crystal structure description of $[Fe_3(\mu_2\text{-bntrz})_6(bntrz)_2(\mu_2\text{-tcnsme})_2](tcnsme)_4{\cdot}4H_2O$ (1·4H$_2$O)

The crystal structure of **1·4H$_2$O** has been solved at 298 and 150 K. The unit cell parameters, crystal and refinement data, and the pertinent bond lengths and bond angles, at both temperatures, are summarized in Tables S1 and S2,† respectively. The asymmetric unit contains two Fe^{II} centres (Fe1 and Fe2), located respectively at the (0 $\frac{1}{2}$ 0) inversion centre (Fe1) and at a general position (Fe2), four bntrz ligands, three $tcnsme^-$ anions and two water molecules, all located at

general positions, giving the general formula of $[Fe_3(\mu_2\text{-bntrz})_6(bntrz)_2(\mu_2\text{-tcnsme})_2](tcnsme)_4{\cdot}4H_2O$ (**1·4H$_2$O**) (Fig. 1). The two Fe^{II} ions (Fe1 and Fe2) display FeN_6 octahedral environments: the Fe1 ion, located at the inversion centre, is coordinated by six bntrz ligands, where every three N-atoms, (N1, N2, N3) and ($N1^{(a)}$, $N2^{(a)}$, $N3^{(a)}$), are connected at the same time to Fe2 and $Fe2^{(a)}$ ions, respectively (Fig. 1a); the distorted octahedral environment of the Fe2 centre is completed by three nitrogen atoms arising from one terminal bntrz ligand (N7) and from two equivalent $tcnsme^-$ anions (N8 and $N9^{(b)}$), acting as bridging ligands through one of the two $C(CN)_2$ "wings" (Fig. 1b).

Examination of the Fe–N bond distances and N–Fe–N bond angles (see below) allows us to describe the metal environment of both Fe^{II} centres (Fe1 and Fe2) as distorted FeN_6 octahedra. The three Fe1–N bond distances (Fe1–N1, Fe1–N2 and Fe1–N3) which are quite similar at room temperature (Table 1) decrease significantly at low temperature as indicated by the averaged $\langle d_{(Fe1-N)}\rangle$ values depicted in Table 1 (2.047(5) and 1.965(7) Å at 298 and 150 K, respectively). Similar trends are observed for the six Fe–N bonds around the Fe2 centre, located at the general position, with a greater effect of temperature ($d\langle$Fe2–N$\rangle$: 2.133(5) and 1.951(7) Å at 298 and 150 K, respectively). Thus, except for this significant temperature effect which will be discussed below, each coordination octahedron environment exhibits a relatively low distortion with respect to the O_h symmetry as revealed by the low values of the angular distortion parameters (Σ and Θ)[50–53] depicted in Table 1. The molecular structure of **1·4H$_2$O** consists of trinuclear moieties of the formula $[Fe_3(\mu_2\text{-bntrz})_6(bntrz)_2]$ in which six bntrz ligands act with μ_2-bridging coordination modes similar to that described for the compound $[Fe_3(\mu_2\text{-bntrz})_6(tcnset)_6]$ (**2**). The two remaining bntrz ligands are terminally coordinated to the two external Fe2 centres, leading to the trinuclear fragment $[Fe_3(\mu_2\text{-bntrz})_6(bntrz)_2]^{6+}$ (see Fig. 1a).

Such cationic trinuclear fragments are connected to each other by symmetric double cyanocarbanion bridges involving 12-membered metallacycles (see Fig. 1b) along the [100] direction, leading to the alternating chain depicted in Fig. 2 (see also Fig. S14 and Fig. S15†) where the trinuclear units are tilted 16.7° from the [100] direction. The intra-trinuclear Fe···Fe distance (Fe1···Fe2/$Fe2^{(a)}$: 3.770(1) Å at 298 K; 3.638(1) Å at 150 K) is almost similar to the corresponding distances observed in Fe^{II} systems based on the triple bridging triazole ligands such as in 1-D coordination polymers, or in di- and trinuclear complexes.[19–41,47] However, the shortest inter-trinuclear Fe···Fe distances across the μ_2-$tcnsme^-$ ligands are, as

Table 1 Fe–N bond lengths (Å) and the distortion parameters, Σ and Θ (°), for compound **1·4H$_2$O** at 298 and 150 K

Compound	**1·4H$_2$O**	
T/K	298	150
Fe1–N1/$N1^{(a)}$	2.044(5)	1.940(7)
Fe1–N2/$N2^{(a)}$	2.048(5)	1.989(7)
Fe1–N3/$N3^{(a)}$	2.048(5)	1.967(7)
$\langle d_{(Fe-N)}\rangle$	2.047(5)	1.965(7)
$^a\Sigma$	20.8	10.2
$^a\Theta$	56.0	27.7
Fe2–N4	2.113(5)	1.944(6)
Fe2–N5	2.151(5)	1.960(7)
Fe2–N6	2.147(5)	1.957(7)
Fe2–N7	2.135(5)	1.968(7)
Fe2–N8	2.145(6)	1.957(7)
Fe2–$N9^{(b)}$	2.105(6)	1.918(7)
$\langle d_{(Fe-N)}\rangle$	2.133(6)	1.951(7)
$^a\Sigma$	17.3	20.5
$^a\Theta$	58.0	67.1

$^a\Sigma$ is the sum of the deviation from 90° of the 12 *cis*-angles of the FeN_6 octahedron; Θ is the sum of the deviation from 60° of the 24 trigonal angles of the projection of the FeN_6 octahedron onto its trigonal faces.[50–53] Codes of equivalent positions: (a) $-x$, $1-y$, $-z$; (b) $1-x$, $1-y$, $-z$.

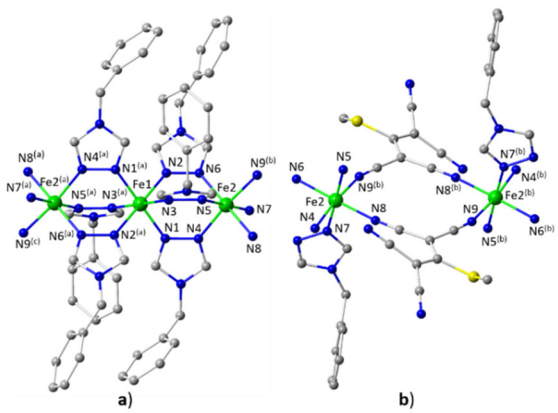

Fig. 1 Perspective view of the trinuclear motif $[Fe_3(\mu_2\text{-bntrz})_6]$ at 150 K (a) and the inter-trinuclear covalent link $(\mu_2\text{-tcnsme})_2$ (b) in **1·4H$_2$O**, showing the asymmetric unit and the coordination environments of the two iron(II) centres (Fe1 and Fe2). Hydrogen atoms have been omitted for the sake of clarity. Codes of equivalent positions: (a) $-x$, $1-y$, $-z$; (b) $1-x$, $1-y$, $-z$, (c) $-1+x$, y, z.

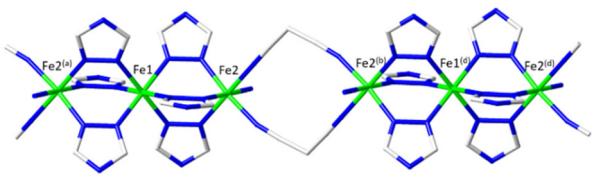

Fig. 2 View of the 1-D alternating chain of $[Fe_3(\mu_2\text{-bntrz})_6(bntrz)_2(\mu_2\text{-tcnsme})_2](tcnsme)_4{\cdot}4H_2O$ (**1·4H$_2$O**), at 150 K, along the [100] direction. Hydrogen atoms, benzyl groups, and part of $(tcnsme)^-$ anions have been omitted for the sake of clarity. Codes of equivalent positions: (a) $-x$, $1-y$, $-z$; (b) $1-x$, $1-y$, $-z$; (d) $1+x$, y, z.

expected, significantly longer, according to the geometry and the rigidity of the $C(CN)_2$ bridging group of the cyanocarbanion coligand (Fe2···Fe2$^{(b)}$: 7.272(1) Å at 298 K; 7.106(1) Å at 150 K). Therefore, the overall molecular structure of **1** is ultimately very different from that of the parent discrete trinuclear complex, $[Fe_3(\mu_2\text{-bntrz})_6(tcnset)_6]$ (**2**), reported previously. This difference arises from the slightly modified cyanocarbanion ($tcnset^-$ in **2**, $tcnsmet^-$ in **1·4H$_2$O**) coligands, which act as terminal ligands in complex **2**, while in complex **1·4H$_2$O**, two $tcnsmet^-$ anions connect two adjacent trinuclear units through a bridging coordination mode implying two nitrile groups from the same $-C(CN)_2$ "wing".

Magnetic properties of $[Fe_3(\mu_2\text{-bntrz})_6(bntrz)_2(\mu_2\text{-tcnsme})_2](tcnsme)_4\cdot 4H_2O$ (1·4H$_2$O)

In the first step, the temperature dependence of the molar magnetic susceptibility (χ_M) was recorded at 0.1 T magnetic field in three consecutive thermal cycles: 50–300–50 K, 50–330–50 K and 50–345–50 K and plotted as $\chi_M T(T)$ in Fig. 3 (the three curves overlap almost perfectly due to good thermal stability of the sample in this temperature range).

The $\chi_M T$ value at 345 K is 9.3 cm^3 K mol^{-1} which corresponds to the situation where almost all Fe^{II} centres are high spin (HS). The relatively low $\chi_M T$ value (3.1 cm^3 K mol^{-1} per Fe^{II}) with respect to that expected for three isolated HS Fe^{II} metal centres can be explained by the fact the $\chi_M T(T)$ dependence of the hydrated phase of **1·4H$_2$O** does not reach the plateau at 345 K. Upon cooling, the $\chi_M T$ value decreases gradually until approximately 230 K reaching a value of 0.55 cm^3 K mol^{-1} which decreases to zero at lower temperatures, in agreement with the presence of a complete and gradual HS to LS transition ($T_{1/2}$ = 281 K), as also revealed by the thermochromism observed on the single crystal (yellow at 298 K and red at 150 K). To estimate the cooperativity in the hydrated phase (**1·4H$_2$O**), we simulated the magnetic spin conversion using the Ising-like model in its mean-field version.[54]

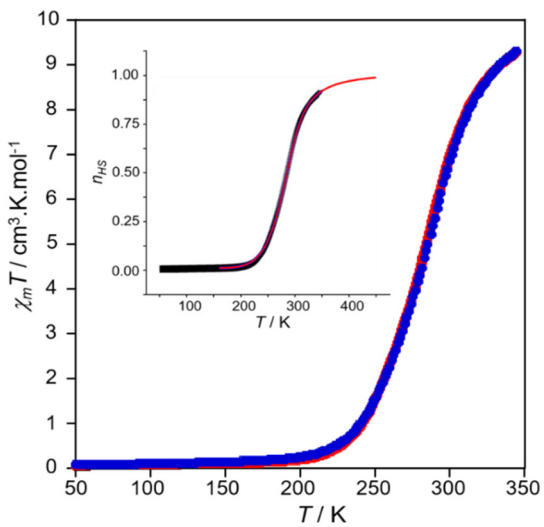

Fig. 3 $\chi_M T(T)$ dependences measured in three consecutive thermal cycles (50–300–50 K, 50–330–50 K and 50–345–50 K) for **1·4H$_2$O**. All points overlap perfectly (blue and red for cooling and heating cycles, respectively). Inset: simulated HS fraction using a mean-field Ising-like model allowing the derivation of the thermodynamic parameters. The red continuous curve corresponds to the best fitting (see the text).

The equation of state of the HS fraction γ_{HS} is given in eqn (1):

$$\ln\left[\frac{1-\gamma_{HS}}{\gamma_{HS}}\right] = \frac{\Delta H + 2\Gamma(1-2\gamma_{HS})}{RT} - \frac{\Delta S}{R}, \qquad (1)$$

where ΔH and ΔS are respectively the enthalpy and the entropy variations at the transition, while Γ is the interaction parameter, of elastic origin, accounting for the cooperative nature of the spin conversion. The HS molar fraction, γ_{HS}, has been deduced from the magnetic susceptibility through eqn (2):

$$\gamma_{HS} = [\chi_M T - (\chi_M T)_{LS}]/[(\chi_M T)_{HS} - (\chi_M T)_{LS}], \qquad (2)$$

where $\chi_M T$ is the value of the effective magnetic moment at any temperature, T, $(\chi_M T)^{HS}$ is the $\chi_M T$ value of the pure HS state ($T \to \infty$), and $(\chi_M T)^{LS}$ is the $\chi_M T$ value of the pure LS. The transition temperature $T_{1/2}$ is the temperature at which γ_{HS} = 0.5 and relates to ΔH and ΔS through $T_{1/2} = \frac{\Delta H}{\Delta S}$. The simulation of the SCO curve of Fig. 3 allowed us to estimate ΔH = 9.644 kJ Mol^{-1}, ΔS = 33 J K^{-1} Mol^{-1} and Γ/k_B = 126 K. According to these values, the transition temperature $T_{1/2} \simeq$ 285 K is larger than the interaction parameter Γ, which explains the gradual character of the transition. The best fitting, presented in Fig. 3 (inset), is based on eqn (2) which was substantially improved by considering a slight HS fraction-dependence of the interaction parameter, Γ, which is expanded to 2nd order with respect to γ_{HS}, such as $\Gamma = \Gamma_0 + a\gamma_{HS} + \frac{1}{2}b\gamma_{HS}^2$, with Γ_0 = 125 K, and $a = b$ = 40 K. This form allows us to better reflect the non-linear character of the HS fraction curve, probably resulting from the presence of short- and long-range interactions, respectively, attributed to intra- and inter-trimer effect couplings.

Magnetic properties of the dehydrated phase (1)

As long as the sample temperature was kept below 345 K, the compound remained in the pristine state (no crystallization solvent loss) and it showed a "stable" $\chi_M T(T)$ dependence with a slightly gradual SCO transition involving almost all Fe^{II} centres and does not show thermal hysteresis nor step-like features (Fig. 3). In the second step, we have performed three additional consecutive thermal cycles by heating gradually the sample to reach the complete HS state of **1·*x*H$_2$O**. Accordingly, when the sample was heated up to 360 K, the two consecutive $\chi_M T(T)$ cycles (50–360–50 K) induced significant shifts of the $\chi_M T$ product towards lower temperatures (see blue and red $\chi_M T$ product curves for the two consecutive thermal cycles 50–360–50 K), suggesting continuous crystallization solvent loss in each cycle (Fig. 4). To stabilize the shift of the $\chi_M T$

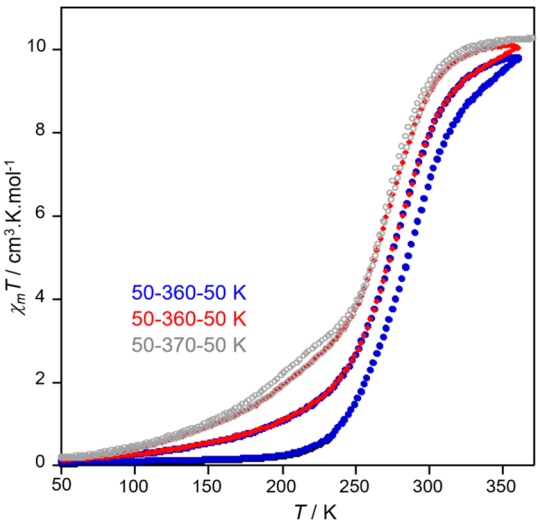

Fig. 4 $\chi_M T(T)$ dependence at 0.1 T of the continuous solvent loss of **1·4H$_2$O**, measured in three consecutive thermal cycles 50–360–50 K (blue), 50–360–50 K (red) and 50–370–50 K (grey) with 2 K min^{-1} scan rate. The points do not overlap due to the continuous solvent loss during the two thermal cycles.

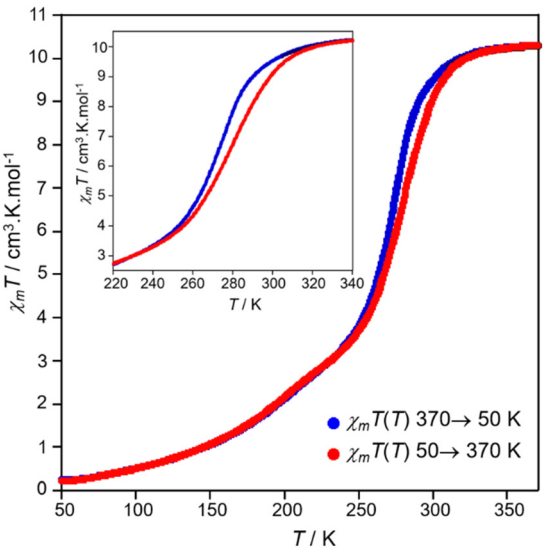

Fig. 5 $\chi_M T(T)$ dependence at 0.1 T, for the dehydrated complex **1**, measured in the final 50–370–50 K thermal cycle (cooling – blue, heating – red) with 2 K min^{-1} scan rate. Inset: the $\chi_M T$ *versus* temperature plot showing the hysteresis loop.

product towards lower temperatures for the cooling and heating scans, we have performed a third thermal cycle by pursuing the gradual scan heating up to 370 K. The resulting behaviour (see the grey $\chi_M T(T)$ curve in Fig. 4) stabilized after heating the sample to 370 K and the final "stable" $\chi_M T(T)$ dependence reached a clear plateau at 370 K with $\chi_M T$ = 10.3 cm^3 K mol^{-1} corresponding to three isolated HS Fe^{II} centres (3.4 cm^3 K mol^{-1} per Fe^{II} which is expected assuming g_{Fe} = 2.13) present in the fully dehydrated compound **1**. Cooling the sample (fully dehydrated complex **1**) from 370 K to 50 K reveals a step-like behaviour with the step-like feature occurring at *ca.* 245 K and $\chi_M T$ = 3.4 cm^3 K mol^{-1} (Fig. 5). The first high-temperature SCO step with $T_{1/2}$ = 270 K is accompanied by a 9 K-wide hysteresis loop recorded with 2 K min^{-1} scan rate (inset Fig. 5) and corresponds to the HS-to-LS transition of two cooperative Fe^{II} centres ($\Delta\chi T$ = 6.9 cm^3 K mol^{-1}).

The second step at $T_{1/2}$ = 180 K, corresponding to the HS-to-LS transition of the third Fe^{II} centre (($\Delta\chi T$ = 3.2 cm^3 K mol^{-1}), is much more gradual and does not show hysteretic behaviour. At 50 K the $\chi_M T$ value drops to 0.2 cm^3 K mol^{-1}, consistent with all Fe^{II} centres in the LS state. However, according to the cooperative character of the first step, it is highly unlikely that this behaviour would be attributed to the two external Fe^{II} centres (Fe2) and the gradual one (second step) to the Fe1 central metal ion (see IR spectroscopy).

Photomagnetic studies of 1·4H$_2$O and 1

Both **1·4H$_2$O** and its dehydrated form **1** comprise two types of Fe^{II} centres ((Fe1(μ_2-bntrz)$_6$) and (Fe2(bntrz)$_4$(NC)$_2$) and therefore we decided to test the possibility of selective photomagnetic switching.[55–57] A small amount of **1·4H$_2$O** (*ca.* 0.8 mg) was spread between two layers of Scotch tape (d = 5 mm) and inserted into a plastic straw. Then the sample was inserted into MPMS cooled to T = 250 K and subjected to five gas–vacuum cycles. This procedure was followed by heating to 300 K and the magnetic susceptibility was recorded at 0.1 T upon cooling to 2 K. The obtained $\chi_M T$ curve is identical to that obtained in the bulk measurement (Fig. S16†), confirming the preservation of the fully hydrated form **1·4H$_2$O**. The temperature was stabilized at 10 K and the sample was irradiated with visible light, but no photomagnetic response was observed at 638 nm nor at 450 nm (power density: P = 6–10 mW cm^{-2}). This can be explained by a very fast relaxation of the photo-induced metastable HS state, as can be expected for **1·4H$_2$O** characterised by $T_{1/2}$ = 281 K based on the empirical formula proposed by Létard:[58]

$$T_{LIESST} = T_0 - 0.3T_{1/2} \quad (3)$$

where T_{LIESST} is the temperature of thermal relaxation of the photo-induced HS state and T_0 is an empirical constant, which for Fe^{II} coordinated by six independent ligands is expected to be around 100 K. Thus, the resulting T_{LIESST} would be around 15 K, precluding the observation of the metastable HS state on the time scale of the SQUID magnetometer measurement. On the other hand, dehydrated **1** shows very gradual SCO behaviour below 250 K with $T_{1/2} \approx$ 180 K, which should make at least some Fe^{II} centres responsive to visible light. Therefore, a sample of **1·4H$_2$O** transformed into **1** inside the magnetometer by vacuum pumping at 345 K was cooled to 10 K and subjected to 638 nm light irradiation. The dehydrated **1** shows a fast increase of magnetization, reaching the plateau of 1.3 cm^3 K mol^{-1} in 30 minutes of irradiation at 20 mW cm^{-2} (Fig. 6).

Turning the light off leads to a sudden increase of magnetization up to 1.55 cm^3 K mol^{-1} due to the sample cooling

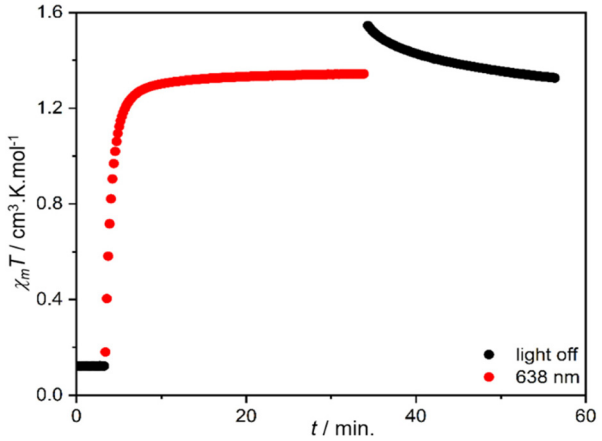

Fig. 6 $\chi_M T(t)$ dependence recorded for **1** at 10 K under 638 nm irradiation at 0.1 T.

during the thermalization process. This sudden increase of the magnetization reflects the existence of photo-heating effects under permanent light irradiation, where the sample is heated well above the 10 K temperature indicated by the controller. Here, from the jump $\Delta(\chi_M T) \sim 0.25$ cm^3 K mol^{-1} observed in Fig. 6, we estimated using Curie's law that the sample's temperature increased under light by about ~2 K. Switching off the light is followed by the slow relaxation of magnetization down to 1.3 cm^3 K mol^{-1} after 20 minutes, thus almost reaching the same value of the magnetic moment at saturation obtained under light. After the episode of photexcitation at 10 K, the sample is cooled down to 2 K and then heated up to 80 K (see Fig. 7) at 0.67 K min^{-1} heating rate. The thermal evolution of the magnetic moment, recorded for the photo-irradiated sample, first increases and shows a maximum of 1.4 cm^3 K mol^{-1} at 22 K (Fig. 7, red line). This first regime, ranged

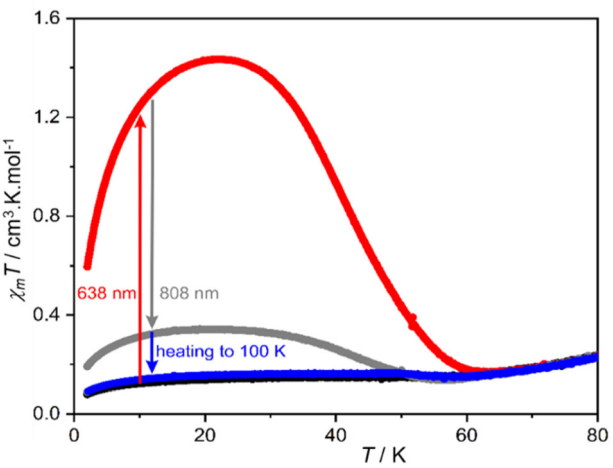

Fig. 7 $\chi_M T(T)$ dependence obtained for **1** at 0.1 T before light irradiation (black), after 638 nm irradiation (red), after 638 nm irradiation followed by 808 nm light (grey) and after light irradiation followed by heating to 100 K (blue). Heating rate: 0.67 K min^{-1}.

between 2 and 22 K, is ascribed to the existence of the expected magnetic anisotropy (zero-field splitting) in paramagnetic trimers of configurations having one or two HS isolated sites (HS–LS–LS, LS–LS–HS or HS–LS–HS), randomly distributed inside the lattice. However, the presence of photo-excited antiferromagnetic species involving two HS nearest-neighbour sites within the trimer (LS–HS–HS or HS–HS–LS), although less probable due to the existence of a huge elastic energy barrier for the central site, cannot be totally excluded. Further heating leads to thermally-induced HS to LS relaxation with T_{LIESST} = 41 K (Fig. S17†) and that for $T_{1/2}$ = 180 K would yield T_0 = 95 K, very close to the anticipated value of T_0 = 100 K for six independent ligand molecules surrounding the metastable HS centre.

The photo-induced HS state in **1** was also tested for the presence of the reverse-LIESST effect.[59–61] When 638 nm irradiation is followed by illumination with infra-red light (λ = 808 nm), a fast decrease of $\chi_M T$ down to 0.3 cm^3 K mol^{-1} is observed. This effect is reversible in at least three 638 nm–808 nm cycles (Fig. S18†). The intermediate HS state obtained after 808 nm de-excitation shows exactly the same thermal relaxation behaviour as the metastable state obtained by 638 nm irradiation (Fig. 7 and Fig. S19,† grey points). This confirms that 808 nm irradiation indeed promotes the reverse-LIESST effect in **1**. However, in order to achieve complete HS-*to*-LS relaxation in **1**, 808 nm irradiation must be followed by heating to 100 K, which completely regenerates the original $\chi_M T(T)$ dependence recorded for the non-irradiated sample (Fig. 7 and Fig. S19,† blue points).

Magneto-structural and spectroscopic relationships

The crystal structure of **1·4H$_2$O** has been solved at 298 and 150 K (see Tables S1 and S2†), but according to the magnetic observations detailed above, ideally, the structural characterisation should have been also studied above 345 K to reach the HS of the hydrated compound. Unfortunately, the present compound shows a low diffracting power above room temperature that arises from the gradual loss of the water solvent molecules (see TGA analysis below and Fig. S20†), thus precluding any correct structural characterisation at high temperature.

It is well known that in Fe^{II} SCO complexes, the LS and the HS spin states can be identified from the thermal evolution of the average Fe–N distances, which are shortened by *ca.* 0.2 Å when the Fe^{II} switches from the HS to the LS state, and by the significant modification of the distortion of the FeN$_6$ coordination octahedron. Table 2 lists the average values of the Fe–N

Table 2 Average Fe–N distances (Å) for **1·4H$_2$O** and **2**

Compound		**1·4H$_2$O**		**2**	
T/K		298	150	360	250
Fe1	$\langle d_{(Fe-N)} \rangle$	2.047(5)	1.965(7)	2.175(2)	1.979(2)
	Spin state	HS/LS	LS	HS	LS
Fe2	$\langle d_{(Fe-N)} \rangle$	2.133(6)	1.951(7)	2.158(3)	1.949(3)
	Spin state	HS/LS	LS	HS	LS

bond lengths for both Fe^{II} centres (Fe1 and Fe2) for **1·4H$_2$O** at 298 and 150 K and for the discrete parent trinuclear complex $[Fe_3(\mu_2\text{-bntrz})_6(tcnset)_6]$ (**2**).[47] According to the molecular structure based on two different Fe^{II} ion centres (Fe1 and Fe2) constituting the trinuclear units, one can expect a two-step SCO behaviour. However, the thermal magnetic response reveals a complete one-step transition, suggesting a concerted transition as already observed in the parent discrete trinuclear complex, $[Fe_3(\mu_2\text{-bntrz})_6(tcnset)_6]$ (**2**).[47]

This observation is clearly supported by the structural data since at 298 K, the Fe–N average bond lengths (2.047(5) Å for Fe1, and 2.133(6) Å for Fe2) suggest the occurrence of intermediate HS/LS phases that should be predominantly LS for the central Fe1 ion and HS for the two external Fe2 centres, while at 150 K the corresponding Fe–N bond lengths (1.965(7) Å for Fe1, and 1.951(7) Å for Fe2) are consistent with a full LS state for each Fe^{II} centre, in agreement with the magnetic data. Furthermore, assuming that the respective averaged ⟨Fe–N⟩ values of 2.18 and 1.98 Å are associated with the full HS and LS states,[14–18] and the $\chi_M T$ value is 10.3 cm^3 K mol^{-1} for the full HS trinuclear unit, the HS fraction at 298 K deduced from the bond length analysis of each metal centre (33.5% for Fe1, and 66.5% for Fe2) leads to a $\chi_M T$ value of 6.40 cm^3 K mol^{-1}, in excellent agreement with that of 6.37 cm^3 K mol^{-1} at 298 K.

As detailed above, when the sample of **1·4H$_2$O** was heated up to 370 K, a different $\chi_M T$ behaviour exhibiting a step-like feature at *ca.* 245 K and $\chi_M T$ = 3.4 cm^3 K mol^{-1} was observed (see Fig. 5); the first step ($T_{1/2} \approx 270$ K), from 10.3 to 3.4 cm^3 K mol^{-1}, corresponding to the HS/LS transition of a $\chi_M T$ signal close to that expected for two Fe^{II} ions (10.3–3.4 = 6.9 cm^3 K mol^{-1}), is accompanied by a hysteresis loop of 9 K, while the second one occurring from 3.4 to 0.2 cm^3 K mol^{-1}, more gradual ($T_{1/2} \approx 180$ K), corresponds to the HS/LS transition involving one Fe^{II} centre of a $\chi_M T$ signal of 3.2 cm^3 K mol^{-1}. This different behaviour, induced by a dehydration of the sample, could not be elucidated by means of single-crystal X-ray diffraction because the crystal structure could not be determined for the dehydrated sample. In order to shed light on the total or partial dehydration of the sample at 370 K and on its reversibility, we have attempted hydration of the same sample used for the magnetic studies after the measurements up to 370 K by soaking it in water and performed simultaneously magnetic studies, powder X-ray diffraction and TGA analysis. The magnetic data obtained in the 10–345 K temperature range for the rehydrated sample show a complete restoration of the original SCO behaviour of **1·4H$_2$O** (Fig. S21†), with slight differences that could be attributed to the change in the crystallinity of the compound induced by the dehydration–rehydration process. TGA analysis (Fig. S20†) reveals that the compound undergoes dehydration readily and the process starts even at room temperature at *ca.* 20 °C and is basically complete around 60 °C, proving that the "hydration (**1·4H$_2$O**)/dehydration (**1**)" process of this sample is reversible and supporting that the high temperature magnetic behaviour (Fig. 5) is the signature of the fully dehydrated sample **1**. Note that the temperature of 345 K designated as "safe" regarding the dehydration of the compound in the magnetic measurement section corresponds to a sample that is sealed inside a double foil bag to protect it from losing the crystallization solvent molecules inside the evacuated sample chamber of the magnetometer. And finally, the powder X-ray diffraction (PXRD) experiments depicted in Fig. 8 show that the pattern recorded after the TGA experiment up to 100 °C for the dehydrated **1** (thermal dehydration; red line) is different from the one simulated from the single-crystal structural model (gray line) for the hydrated compound **1·4H$_2$O**. However, rehydration by soaking the anhydrous sample (thermally dehydrated sample) in water restores almost completely the initial state as evidenced by the corresponding PXRD pattern (green line in Fig. 8). The PXRD diagram of the rehydrated compound almost perfectly matches that of the pristine single crystal of **1·4H$_2$O** (gray line in Fig. 8). The diagram of the rehydrated compound can be well reproduced with the calculated diagram of the pristine single crystal of **1·4H$_2$O** with a small amount of the anhydrous phase (Fig. S22†). These observations clearly suggest the occurrence of a reversible structural phase transition. According to the easy reversibility of the "hydration/dehydration" process occurring at relatively low temperature, the presumed structural transition induced by the dehydration should not affect strongly the crystal structure described for the hydrated phase even if the experimental powder X-ray diffraction patterns observed for the hydrated and dehydrated samples are different. Furthermore, the PXRD diagram of the dehydrated phase could be well reproduced by profile matching using a similar unit cell with the following monoclinic parameters: a = 13.749 Å, b = 22.826 Å, c = 21.021 Å and β = 106.265° (Fig. S23†). As almost all the peaks are well fitted by this unit cell, it should be close to the real one with, maybe, a lower symmetry such as a non-centrosymmetric monoclinic space group ($P2_1$ or Pn). Therefore, only slight structural changes are

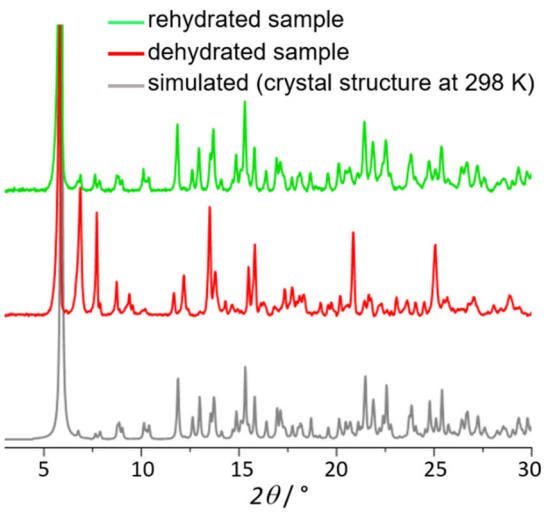

Fig. 8 Experimental PXRD patterns for the hydrated (**1·4H$_2$O**) and dehydrated (**1**) phases, and the simulated pattern derived from the crystal structure of **1·4H$_2$O** at 298 K.

expected, in agreement with the easy "hydration/dehydration" process.

In order to better understand the thermal evolution of the overall spin state of the three Fe^{II} centres, but also and more importantly to know more on the distinct thermal dependence of each type of the Fe^{II} centres (two external ions, Fe2 and one central Fe1 ion), as well as the origin of the two-step behavior of the dehydrated phase of **1**, we have performed thermal dependence infrared spectroscopy in the 2200–2220 cm^{-1} range corresponding to the fundamental stretching vibration of the NC groups for the dehydrated sample (**1**), since it is well known that the intensities of these stretching vibrations are very sensitive to the spin state of the metal ion.[43,62–71] According to the crystal structure which reveals clearly that only the two external Fe^{II} ions are covalently linked to the CN groups, this experiment seems to be of major importance since the thermal evolution of the fundamental stretching vibration of these nitrile groups should get the temperature range corresponding to the HS/LS region of the two external and equivalent metal ions (Fe2 and $Fe2^{(a)}$), which will allow correct extraction of the magnetic behaviour related to these two centres and therefore the thermal evolution of the spin state of the central Fe^{II} ion (Fe1). In line with the thermal dependence of the $\chi_M T$ product depicted in Fig. 5, we have studied the fundamental stretching vibration of the NC groups belonging to the $tcnsme^-$ bridging ligand for the dehydrated sample (**1**) in the temperature range 370–100 K. The final infrared spectra in the 2200–2220 cm^{-1} range are depicted in Fig. 9. At 100 K, the infrared spectrum shows two large strong bands (2205 and 2214 cm^{-1}) which are characteristic of the LS state, while at 345 K, corresponding to almost the HS state region, only a weak broad band centred around 2208 cm^{-1} was observed (Fig. 9a). Thus, this observation prompted us to favour the thermal evolution of the characteristic bands of the LS state for the following discussion in the restricted temperature range 310–100 K since above 310 K the vibrational infrared bands could not be pointed correctly (see red lines in Fig. 9b: infrared spectra for **1** in the temperature range 320–370 K). On heating the sample, the two strong bands observed at 100 K decrease and shift gradually to lower wavenumbers up to 310 K (see blue and green lines in Fig. 9b) where they became very weak and almost undetectable at higher temperatures (see red lines in Fig. 9b), in agreement with the presence of almost 100% HS state above 310 K (see Fig. 5).

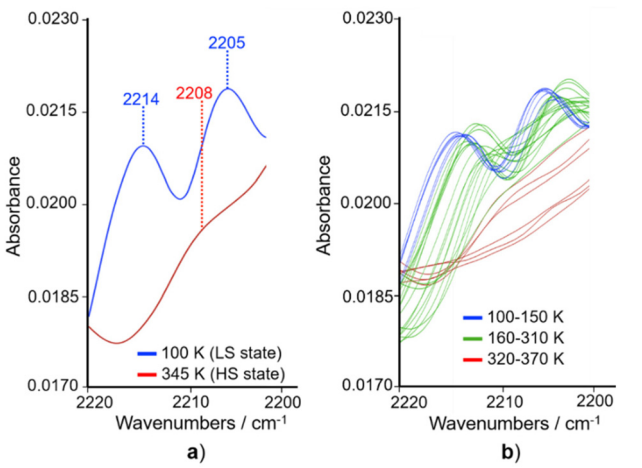

Fig. 9 Infrared spectra for the dehydrated sample (**1**) in the 2200–2220 cm^{-1} region: (a) absorption bands observed at 345 K and at 100 K for the HS and LS states, respectively; (b) temperature dependences of the infrared spectra in the temperature region 370–100 K.

To study the global consistency of the experimental data derived from the thermal dependence of infrared spectroscopy, we have correlated the thermal-dependence of the $\chi_M T$ product and those of the thermal evolution of the relative intensity of the two infrared bands (2205 and 2214 cm^{-1}) characteristic of the LS state of the two external Fe^{II} ions (Fe2) covalently linked to the nitrile groups, since it is expected, from the molecular structure of **1**, that the absorbance of the two vibrational bands should not be affected significantly by the presence of the central Fe^{II} ion (Fe1) for which the coordination environment does not involve nitrile groups. Considering the temperature range 100–310 K in which the infrared spectra have been recorded, we have juxtaposed the relative absorbance (1-ABS) *vs.* *T* of both vibrational band plots (2205 and 2214 cm^{-1}) with the thermal evolution of the $\chi_M T$ product corresponding to the cooling scan (370–50 K) performed on the dehydrated phase (**1**). The best consistency corresponds to the resulting behaviour depicted in Fig. 10 (see purple dots) for the band observed at 2205 cm^{-1} (see Fig. S24† for the band observed at 2214 cm^{-1}). This observation evidences that the two external Fe^{II} ions (Fe2 centres) are HS at 310 K ($\chi_M T \approx 6.8$ cm^3 K mol^{-1}) and the corresponding HS-to-LS transition starts around 290 K, reaching an almost complete LS state below 100 K. Accordingly, an estimation of the switching behaviour of the central Fe^{II} ion (Fe1) can be obtained by subtracting the magnetic contribution of the two Fe2 ions (purple plot in Fig. 10) from the total $\chi_M T(T)$ plot (blue plot in Fig. 10) derived from the squid measurements. This led to the plot depicted in Fig. 10 (see green dots), indicating a $\chi_M T$ value of *ca.* 3.0 cm^3 K mol^{-1} at 310 K, revealing that the SCO transition of Fe1 is more cooperative, occurs at higher temperature (>310 K) with an estimated HS $\chi_M T$ value of 3.5 cm^3 K mol^{-1} (10.3–6.8 = 3.5 cm^3 K mol^{-1}) at 370 K, a transition temperature of *ca.* 280 K and an almost complete LS state below 255 K.

Finally, the conclusion derived from such a magneto-spectroscopic study allows us to reconsider the discussion related to the two-step behaviour discussed above (high- and low-temperature SCO steps with a transition temperature of 270 and 180 K, respectively) for the dehydrated sample (**1**). The first step (370–245 K, $T_{1/2}$ = 270 K) accompanied by a 9 K-wide hysteresis loop (inset Fig. 5), corresponding to the abrupt part of the overall transition, was initiated by the HS-to-LS transition of the central Fe^{II} ion (Fe1): in the temperature range 370–290 K, the two external centres are HS (see Fig. 10) and therefore, the corresponding $\chi_M T$ decrease (from 10.3 cm^3 K mol^{-1} at 370 K to 9.0 cm^3 K mol^{-11} at 290 K) is exclusively

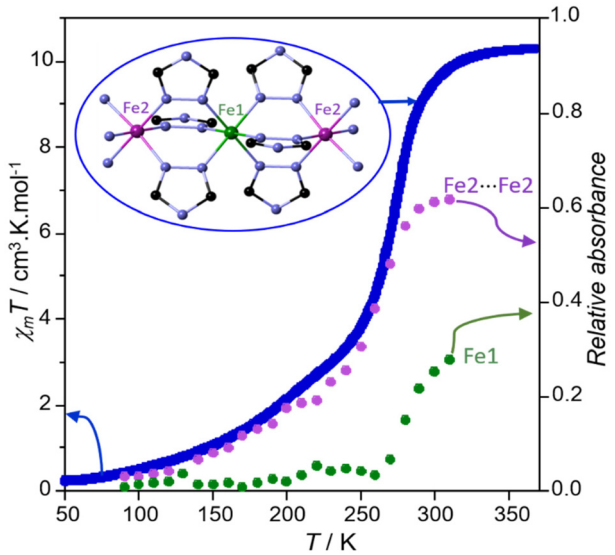

Fig. 10 Temperature dependence of the relative absorbance of the ν(CN) band observed at 2205 cm^{-1} (●) in correlation with the $\chi_M T$ product (● cooling scan) derived from the magnetic data for the dehydrated sample (**1**). Similar correct correlation for the relative absorbance ((1-ABS) *vs.* *T*) of the $\nu_{C\equiv N(LS)}$ bands observed at 2214 cm^{-1} is also observed (see Fig. S24†). The thermal evolution of the absorbance of the $\nu_{C\equiv N}$ band attributed to the central Fe1 centre (●) was derived by subtracting the plot of the relative absorbance of the ν(CN), attributed to the two external Fe2 centres, from the total $\chi_M T$ plot observed for the dehydrated sample (**1**). Inset: the molecular structure of the trinuclear unit showing the coordination environment of Fe1 (Fe1(μ_2-bntrz)$_6$) and Fe2 (Fe2(bntrz)$_4$(NC)$_2$) centres.

induced by the HS-to-LS switching of a fraction of the central Fe^{II} centre (Fe1). Below 290 K, where the transition displays a much more abrupt character, the HS-to-LS transformation of the two external Fe^{II} ions (Fe2) starts and continues concomitantly with that of the central Fe1 ion up to 245 K, where the SCO transition of the Fe1 centre is almost completed. However, and according to the magnetic data (Fig. 10), it appears that the switching of the central metal centre (Fe1) drives only the half of the external Fe2 ions to convert to the LS state which most likely takes place randomly in the lattice.

This means that this first step can be attributed to the conversion of full HS trimers to the Fe2(HS)–Fe1(LS)–Fe2(HS) configuration which is concomitantly followed by a transition to a disordered phase where only 50% of Fe2 sites switch to the LS state leading to a mixing phase made of Fe2(LS)–Fe1(LS)–Fe2(HS) and Fe2(HS)–Fe1(LS)–Fe2(LS). Indeed, the occurrence of ordered domain growth from Fe2(HS)–Fe1(HS)–Fe2(HS) to Fe2(LS)–Fe1(LS)–Fe2(LS) would face to a very high elastic energy originating from the inter-trimer elastic interactions. Thus, below 245 K, the remaining HS state among the randomly distributed Fe2 external ions switches very gradually to the LS state up to 50 K, as clearly revealed by the decrease of the $\chi_M T$ product of the dehydrated sample (**1**) and by that of the relative infrared absorbance attributed to the external Fe2 centres (see purple dots in Fig. 10). Indeed, the shape of the magnetic and absorbance curves (Fig. 10) below 245 K is characteristic of the transformation of a disordered phase, made of connected inter-trimer Fe2 centres (see Fig. 1b), with the presence of distributed local deformations renormalizing locally the effective ligand field energy felt by the HS Fe2 metal sites. This effect causes the spreading of the transition temperatures, from which originates the stretched shape of the transition curve below 245 K. This gradual second step implying the absence of significant cooperative effects is consistent with the observation of a HS photo-induced spin state for this dehydrated phase (**1**) which thus can be attributed to the photo-conversion of a fraction of one of the two randomly distributed external Fe^{II} centres (Fe2). Overall, these plausible mechanisms explain the emergence of the two-step character of the transition with the presence of two regimes in the thermal transition.

A final important aspect of the present work concerns the structural differences between the alternating covalent chain of trinuclear units described for the fully hydrated **1·4H$_2$O** and the discrete neutral trinuclear complex of **2** previously reported by some of us.[47] As expected, both complexes display an almost similar trinuclear unit [Fe$_3$(μ_2-bntrz)$_6$] consisting of three Fe^{II} ions connected covalently by three bridging triazole ligands ([Fe$_3$(μ_2-bntrz)$_6$]) (Fig. 11). Nevertheless, the main structural difference should arise from the nature of the interactions involved between adjacent trinuclear units in each molecular system along the covalent chain ([100] direction) for **1·4H$_2$O** and along the [001] direction for **2**.[47] Careful examination of the interchain contacts in **1·4H$_2$O** reveals, as for **2**, very weak interchain interactions (see Table S3†). This confirms that the spin states and consequently the magnetic properties are essentially controlled by the antagonist elastic interactions within the chain of trimers described in both systems. As detailed above for **1·4H$_2$O**, the trinuclear fragments are connected to each other by symmetric double cyanocarbanion bridges ((μ_2-tcnsme)$_2$), while for complex **2**, involving a slightly modified cyanocabanion (tcnset$^-$) acting as a terminal ligand, has been described as a 1-D chain based on the hydrogen bond contacts between trinuclear units (see Fig. 11).

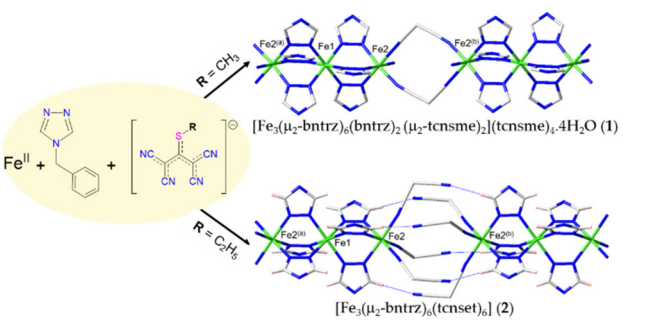

Fig. 11 1-D alternating covalent chain of (**1·4H$_2$O**). View of the 1-D chain of **2** based on the hydrogen bond contacts between trinuclear units. Codes of equivalent positions: (a) $-x$, 1 $-$ y, $-z$ (**1**) and 2/3 $-$ x,4/3 $-$ y,4/3 $-$ z (**2**); (b) 1 $-$ x, 1 $-$ y, $-z$ (**1**) and 2/3 $-$ x,4/3 $-$ y,1/3 $-$ z (**2**).

Consequently, complex **2** seems to be more flexible than complex **1·4H$_2$O** in which the trinuclear units are linked covalently. Indeed, examination of the structural unit in both complexes reveals intramolecular Fe1···Fe2 distances for the full LS state (3.638(1) Å for **1·4H$_2$O** and 3.657(1) Å for **2**, at 150 and 250 K, respectively), even if the corresponding values at high temperature (3.770(1) Å for **1·4H$_2$O** at 298 K, and 3.865(1) Å for **2** at 360 K) are significantly different due to the HS state that is not completely reached at 298 K for **1·4H$_2$O**, as revealed by the magnetic data. In both cases, the trinuclear units show significant contractions from the HS to the LS states, in agreement with that expected from their SCO behaviour. In contrast, the evolution of the Fe···Fe inter-trinuclear distances (Fe2···Fe2$^{(b)}$) along the covalent chain in **1·4H$_2$O** and along the [001] direction for **2** shows completely opposite tendencies, since in complex **1·4H$_2$O** the Fe2···Fe2$^{(b)}$ decreases from 7.272 (1) Å for the HS to 7.106(1) Å for the LS spin state, while for the discrete trinuclear complex (**2**) this value increases from 7.094(1) Å at 360 K to 7.419(1) Å at 250 K (Table 3). Clearly, for **2**, the contraction of the trimers at low temperature due to the HS to LS transition led to the elongation of the distance between the trimers (from 7.094(1) Å for the HS state to 7.419 (1) Å for the LS state) as they are not strongly connected to each other.

Conversely, for **1·4H$_2$O**, cyanocarbanion coligands covalently connect the trimers, which leads to a reduction of the distance between trimers due to the shortening of the Fe–N bond of the bridging ligand. This shortening of the distance is then accompanied by a higher distortion of the Fe^{II} octahedron at low temperature despite the low spin state due to the constrain of the bridge. Noteworthily, the Fe^{II} environment in **1·4H$_2$O** shows globally higher distortion than in **2**, which may explain the lower $T_{1/2}$ even if the slight difference in the cyanocarbanion (Me *vs.* Et groups) may also explain the difference through a small modification of the ligand field. The higher distortion observed on Fe2 sites may also explain that Fe2 undergoes SCO at a lower temperature than Fe1. One should note that the increase of the inter-trimer (Fe2···Fe2$^{(b)}$) distances in complex **2** along the HS to LS transition clearly means that the trinuclear units react as a single body along the SCO transition. It also suggests that the elastic interaction, of ferroelastic nature in **2**, inside the trimer is stronger than that acting between the trimers, which is in line with the weak hydrogen bond nature of the contacts between trinuclear units. Thus, the decrease of the intra-trimer distances on cooling is not counterbalanced by the inter-trimer elastic energy that would prevent this structural transformation. If the interaction between the trimers was negligible in complex **2** their distance (Fe2···Fe2$^{(b)}$) would increase by 0.416 Å (see Table 3) along the HS to LS conversion, while the latter increases by 0.325 Å, which constitutes 78% of the maximum allowed inter-trimer distance expansion. In contrast, complex **1·4H$_2$O** exhibits a decrease of both intra- and inter-trinuclear distances along the HS to LS transition. This behaviour denotes that the trimers are strongly linked by the covalent bonds. As a result, the conversion of the central ion (Fe1) in each trimer decreases the Fe1···Fe2 distance by only 0.132 Å compared to the corresponding distance of 0.208 Å for complex **2**. The anti-ferroelastic interactions between the trimers, in **1·4H$_2$O**, hinder the increase of the inter-trimer distance on cooling, contrary to what was observed in complex **2**. Indeed, in complex **1·4H$_2$O**, the inter-trimer distance decreases by about 0.166 Å along the HS to LS transition.

Thus, the Fe2 metal centres of complex **1·4H$_2$O** are subject to antagonist and competing interactions while in complex **2** these atoms are less sensitive to the steric effects of the inter-trimer interactions. Last but not least, this discussion based on the hydrated phase (**1·4H$_2$O**) and on the discrete trinuclear complex (**2**) can be extended to the dehydrated phase for which the crystal structure could not be determined. Indeed, as mentioned above, powder X-ray diffraction (PXRD) experiments performed on the dehydrated sample (**1**) revealed unit cell parameters (a = 13.749 Å, b = 22.826 Å, c = 21.021 Å and β = 106.26°) while those of the hydrated phase **1·4H$_2$O** can be seen in Table S1:† a = 14.073 Å, b = 22.411 Å, c = 21.028 Å and β = 106.60°. This observation is consistent with the presence, in the dehydrated phase (**1**), of a 1-D chain running along the [100] direction, similar to that derived from the single crystal diffraction of the hydrated phase (see Fig. 2). In addition, the a parameter in **1** (13.749 Å) appears significantly (2.3%) shorter than that observed for **1·4H$_2$O** (14.073 Å). Thus, considering the Fe···Fe distance constant within the trinuclear complex (see Fe1···Fe2 and Fe1···Fe2$^{(a)}$ in Fig. 2), as observed in the similar trinuclear complexes based on the [Fe$_3$(R-trz)$_6$] rigid motif, one can assume that the shortening of the a parameter ($\sim$ 0.32 Å) in the dehydrated phase (**1**) will essentially impact the distance between the trinuclear units (see Fe2···Fe2$^{(b)}$ in Fig. 2). Consequently, the alternating chain of trinuclear units in **1** with shorter inter-trinuclear distances will probably be subjected to stronger elastic interactions than those expected for the hydrated phase (**1·4H$_2$O**). This observation implies the occurrence of elastic frustration resulting from the existence of antagonist elastic interactions.[72] The presence of a step-like SCO transition in **1** suggests the presence of an interplay between ferroelastic intra-trimer and anti-ferroelastic inter-trimer interactions, having the same order of magnitude, and competing in the alternating chain of trimers.

Table 3 Distortion parameters, Σ and Θ (°), and Fe···Fe intra and inter-trinuclear distances (Å) for **1·4H$_2$O** and **2**

Compound		**1·4H$_2$O**		**2**	
T/K		298	150	360	250
Spin state		HS/LS	LS	HS	LS
Fe1	Σ(°)	20(4)	10(3)	8(1)	4(1)
	Θ (°)	56(7)	27(5)	9(2)	5(2)
Fe2	Σ(°)	17(4)	20(3)	24(1)	8(1)
	Θ (°)	58(7)	67(5)	39(2)	14(2)
d(Fe1···Fe2)		3.770(1)	3.638(1)	3.865(1)	3.657(1)
d(Fe2···Fe2$^{(b)}$)		7.272(1)	7.106(1)	7.094(1)	7.419(1)

Conclusions

This work reports a detailed study on the new 1D coordination polymer $[Fe_3(\mu_2\text{-bntrz})_6(bntrz)_2(\mu_2\text{-tcnsme})_2](tcnsme)_4{\cdot}4H_2O$ (**1·4H$_2$O**), based on the $[Fe_3(\mu_2\text{-bntrz})_6]$ trinuclear units covalently linked by symmetric double cyanocarbanion coligands involving 12-membered metallacycles. The crystal structure of **1·4H$_2$O**, solved at 298 and 150 K, revealed that the trinuclear $[Fe_3(\mu_2\text{-bntrz})_6(bntrz)_2(\mu_2\text{-tcnsme})_2]^{4+}$ unit, similar to that described for the discrete trinuclear complex $[Fe_3(\mu_2\text{-bntrz})_6(tcnset)_6]$ (**2**),[47] is composed of two different Fe^{II} ions with FeN_6 octahedral environments: a central Fe^{II} ion (Fe1) located on the inversion centre and two equivalent external metal ions (Fe2). Magnetic studies of **1·4H$_2$O**, performed in the temperature range 50–345 K, revealed a continuous gradual decrease of the magnetic signal, in agreement with the presence of a complete one-step gradual HS to LS transition ($T_{1/2}$ = 281 K). Such behaviour, different from the abrupt one described for the discrete trinuclear $[Fe_3(\mu_2\text{-bntrz})_6(tcnset)_6]$ (**2**) complex,[47] has been explained by the presence, in **1·4H$_2$O**, of intra- (μ_2-bntrz) and inter-trimer (μ_2-tcnsme) covalent bridges, at the origin of the antagonist and competing ferroelastic intra-trimer and anti-ferroelastic inter-trimer interactions, while in complex **2**, in which the neutral trinuclar units are connected through weak hydrogen bonds, the two external metal ions (Fe2) are less sensitive to the steric effects of the inter-trimer interactions, and therefore the overall elastic effects are dominated by the ferroelastic interactions inside the trimer. Heating the **1·4H$_2$O** sample up to 370 K led to a magnetic behavior, exhibiting a step-like feature at *ca.* 245 K. The first step corresponds to the HS/LS transition ($T_{1/2} \approx$ 270 K) involving two Fe^{II} metal ions accompanied by a hysteresis loop of 9 K, while the second step, much more gradual ($T_{1/2} \approx$ 180 K), corresponds to the HS/LS transition involving one Fe^{II} centre. This peculiar behaviour has been attributed to the complete dehydration of the sample (**1**) on the basis of TGA analysis. Soaking the dehydrated sample (**1**) in water shows a complete restoration of the original SCO behaviour and the XPRD patterns of **1·4H$_2$O**, supporting the reversibility of the "hydration (**1·4H$_2$O**)/dehydration (**1**)" process. According to vibrational IR spectroscopy that allowed correct extraction of the thermal evolution of the spin states related to both Fe^{II} centres (one central Fe1 and two external Fe2 metal ions), the first step corresponding to the abrupt part of the transition (370–245 K, $T_{1/2}$ = 270 K) was clearly attributed to a concomitant HS/LS switching of the central Fe1 and a half of the Fe2 ions, and the second step, occurring below 245 K, was attributed to the HS/LS transition of the remaining HS state among the randomly distributed Fe2 external ions.

It should be noted that besides the fundamental role of the elastic interactions in driving the SCO behaviour, the final objective should be the perfect chemical control of such antagonist intra- and inter-molecular elastic interactions for the design of new switchable systems with desirable SCO behaviour. In this context, we are now using a large series of cyanocarbanion coligands with different functional groups of different steric and electronic effects to achieve control of the intermolecular contacts, including the H-bond strength and covalent links.

Author contributions

N. P. performed all the chemical syntheses (ligands and complexes) under supervision of S. T.; E. C. carried out variable temperature infrared spectroscopy; D. P. performed and analysed the magnetic data, the TGA analysis and the X-ray powder diffraction; M. M. (Krakow) performed and analysed the photomagnetic data under the supervision of D. P.; M. M. (Bordeaux) refined the crystal structures; K. B. modeled the SCO transition and discussed the elastic interactions; S. T. supervised the experimental work and wrote the manuscript in which all the authors have contributed.

Conflicts of interest

There are no conflicts to declare.

Acknowledgements

This research was funded by the French CNRS (MITI Project), Mol-CoSM ANR Project No. ANR-20-CE07-0028-01. NP and EC acknowledge the PhD financial support from "Région de Bretagne and Université de Brest". DP and MM acknowledge the financial support of the Polish National Science Centre within the Opus project no. 2020/39/B/ST5/02815.

References

1 M. P. Cuéllar, A. Lapresta-Fernández, J. M. Herrera, A. Salinas-Castillo, M. del C. Pegalajar, S. Titos-Padilla, E. Colacio and L. F. Capitán-Vallvey, Thermochromic sensor design based on Fe(II) spin crossover/polymers hybrid materials and artificial neural networks as a tool in modelling, *Sens. Actuators, B*, 2015, **208**, 180–187.

2 A. Lapresta-Fernandez, S. Titos-Padilla, J. M. Herrera, A. Salinas-Castillo, E. Colacio and L. F. Capitan-Vallvey, Photographing the synergy between magnetic and colour properties in spin crossover material $[Fe(NH_2trz)_3](BF_4)_2$: A temperature sensor perspective, *Chem. Commun.*, 2013, **49**, 288–290.

3 J. Linares, E. Codjovi and Y. Garcia, Pressure and temperature spin crossover sensors with optical detection, *Sensors*, 2012, **12**, 4479–4492.

4 B. Benaicha, K. Van Do, A. Yangui, N. Pittala, A. Lusson, M. Sy, G. Bouchez, H. Fourati, C. J. Gómez-García, S. Triki and K. Boukheddaden, Interplay between spin-crossover and luminescence in a multifunctional single crystal iron (II) complex: towards a new generation of molecular sensors, *Chem. Sci.*, 2019, **10**, 6791–6798.

5 C. Bartual-Murgui, A. Akou, C. Thibault, G. Molnar, C. Vieu, L. Salmon and A. Bousseksou, Spin-crossover metal–organic frameworks: promising materials for designing gas sensors, *J. Mater. Chem. C*, 2015, **3**, 1277–1285.

6 M. Matsuda, H. Isozaki and H. Tajima, Reproducible on–off switching of the light emission from the electroluminescent device containing a spin crossover complex, *Thin Solid Films*, 2008, **517**, 1465–1467.

7 K. S. Murray and C. J. Kepert, Cooperativity in spin crossover systems: Memory, magnetism and microporosity, *Top. Curr. Chem.*, 2004, **233**, 195–228.

8 A. Galet, A. B. Gaspar, M. C. Muñoz, G. V. Bukin, G. Levchenko and J.-A. Real, Tunable Bistability in a Three-Dimensional Spin-Crossover Sensory-and Memory-Functional Material, *Adv. Mater.*, 2005, **17**, 2949–2953.

9 K. S. Kumar and M. Ruben, Emerging trends in spin crossover (SCO) based functional materials and devices, *Coord. Chem. Rev.*, 2017, **346**, 176–205.

10 J. Dugay, M. Aarts, M. Giménez-Marqués, T. Kozlova, H. W. Zandbergen, E. Coronado and H. S. J. van der Zant, Phase transitions in spin-crossover thin films probed by graphene transport measurements, *Nano Lett.*, 2017, **17**, 186–193.

11 F. Prins, M. Monrabal-Capilla, E. A. Osorio, E. Coronado and H. S. J. van der Zant, Room-temperature electrical addressing of bistable spin-crossover molecular system, *Adv. Mater.*, 2011, **23**, 1545–1549.

12 A. C. Aragonès, D. Aravena, J. I. Cerdá, Z. Acís-Castillo, H. Li, J.-A. Real, F. Sanz, J. Hihath, E. Ruiz and I. Díez-Pérez, Large conductance switching in a single-molecule device through room temperature spin-dependent transport, *Nano Lett.*, 2016, **16**, 218–226.

13 T. Miyamachi, M. Gruber, V. Davesne, M. Bowen, S. Boukari, L. Joly, F. Scheurer, G. Rogez, T. K. Yamada, P. Ohresser, E. Beaurepaire and W. Wulfhekel, Robust spin crossover and memristance across a single molecule, *Nat. Commun.*, 2012, **3**, 938.

14 *Spin-Crossover Materials: Properties and Applications*, ed. M. A. Halcrow, Wiley, 2013.

15 Z.-Y. Li, J.-W. Dai, M. Damjanović, T. Shiga, J.-H. Wang, J. Zhao, H. Oshio, M. Yamashita and X.-H. Bu, Structure Switching and Modulation of the Magnetic Properties in Diarylethene-Bridged Metallosupramolecular Compounds by Controlled Coordination-Driven Self-Assembly, *Angew. Chem., Int. Ed.*, 2019, **58**, 4339–4344.

16 F. El Hajj, G. Sebki, V. Patinec, M. Marchivie, S. Triki, H. Handel, S. Yefsah, R. Tripier, C. J. Gómez-García and E. Coronado, Macrocycle-based spin-crossover materials, *Inorg. Chem.*, 2009, **48**, 10416–10423.

17 M. Shatruk, H. Phan, B. A. Chrisostomo and A. Suleimenova, Symmetry-breaking structural phase transitions in spin crossover complexes, *Coord. Chem. Rev.*, 2015, **289–290**, 62–73.

18 C. Atmani, F. El Hajj, S. Benmansour, M. Marchivie, S. Triki, F. Conan, V. Patinec, H. Handel, G. Dupouy and C. J. Gómez-García, Guidelines to design new spin crossover materials, *Coord. Chem. Rev.*, 2010, **254**, 1559–1569.

19 A. Grosjean, N. Daro, B. Kauffann, A. Kaiba, J.-F. Létard and P. Guionneau, The 1-D polymeric structure of the [Fe(NH2trz)3](NO3)2, nH_2O (with n=2) spin crossover compound proven by single crystal investigations, *Chem. Commun.*, 2011, **47**, 12382–12384.

20 N. Pittala, F. Thétiot, S. Triki, K. Boukheddaden, G. Chastanet and M. Marchivie, Cooperative 1D Triazole-Based Spin Crossover Fe^{II} Material With Exceptional Mechanical Resilience, *Chem. Mater.*, 2017, **29**, 490–494.

21 Y. Garcia, F. Robert, A. D. Naik, G. Zhou, B. Tinant, K. Robeyns, S. Michotte and L. Piraux, Spin transition charted in a fluorophoretagged thermochromic dinuclear iron(II) complex, *J. Am. Chem. Soc.*, 2011, **133**, 15850–15853.

22 X. Cheng, Q. Yang, C. Gao, B.-W. Wang, T. Shiga, H. Oshio, Z.-M. Wang and S. Gao, Thermal and light induced spin crossover behavior of a dinuclear Fe(II) compound, *Dalton Trans.*, 2015, **44**, 11282–11285.

23 J. L. Wang, Q. Liu, Y. S. Meng, H. Zheng, H. L. Zhu, Q. Shi and T. Liu, Synergic on/off photoswitching spin state and magnetic coupling between spin crossover centers, *Inorg. Chem.*, 2017, **56**, 10674–10680.

24 O. Roubeau, P. Gamez and S. J. Teat, Dinuclear Complexes with a Triple N1,N2-Triazole Bridge That Exhibit Partial Spin Crossover and Weak Antiferromagnetic Interactions, *Eur. J. Inorg. Chem.*, 2013, 934–942.

25 X. X. Wu, Y. Y. Wang, P. Yang, Y. Y. Xu, J. Z. Huo, B. Ding, Y. Wang and X. Wang, Syntheses, Structural Variation, and Characterization of a Series of Crystalline Coordination Compounds with 4-Benzene-1,2,4-triazole: Polymorph, Incomplete Spin Transition, and Single Crystal-to-Single Crystal Transformation, *Cryst. Growth Des.*, 2014, **14**, 477–490.

26 B. Ding, Y. Y. Liu, Y. Wang, J.-G. Ma, Z. Niu, W. Shi and P. Cheng, Syntheses, structures and magnetic properties of a series of iron(II)-triazole crystalline coordination compounds: Solvent effect, different substituted groups and incomplete spin transition, *Inorg. Chem. Commun.*, 2013, **31**, 44–48.

27 J. J. A. Kolnaar, M. I. deHeer, H. Kooman, A. L. Spek, G. Schmitt, V. Ksenofontov, P. Gütlich, J. G. Haasnoot and J. Reedijk, Synthesis, Structure and Properties of a Mixed Mononuclear/Dinuclear Iron(II) Spin-Crossover Compound with the Ligand 4-(p-Tolyl)-1,2,4-triazole, *Eur. J. Inorg. Chem.*, 1999, 881–886.

28 W. B. Chen, Y. C. Chen, M. Yang, M. L. Tong and W. Dong, Water molecule induced reversible single-crystal-to-single-crystal transformation between two trinuclear Fe(ii) complexes with different spin crossover behaviour, *Dalton Trans.*, 2018, **47**, 4307–4314.

29 A.-M. Li, T. Hochdörffer, J. A. Wolny, V. Schünemann and E. Rentschler, Abrupt Spin Crossover Behavior in a Linear N1,N2-Triazole Bridged Trinuclear Fe(II) Complex, *Magnetochemistry*, 2018, **4**, 34.

30 W. B. Chen, J. D. Leng, Z. Z. Wang, Y. C. Chen, Y. Miao, M. L. Tong and W. Dong, Reversible crystal-to-crystal trans-

formation from a trinuclear cluster to a 1D chain and the corresponding spin crossover (SCO) behaviour change, *Chem. Commun.*, 2017, **53**, 7820–7823.

31 Y. M. Klein, N. F. Sciortino, C. E. Housecroft, C. J. Kepert and S. M. Neville, Structure and Magnetic Properties of the Spin Crossover Linear Trinuclear Complex $[Fe_3(furtrz)_6(ptol)_2(MeOH)_4]\cdot 4(ptol)\cdot 4(MeOH)$ (furtrz: furanylidene-4H-1,2,4-triazol-4-amine ptol: p-tolylsulfonate), *Magnetochemistry*, 2016, **2**, 7.

32 H. Z. Scott, T. M. Ross, B. Moubaraki, K. S. Murray and S. M. Neville, Spin Crossover in Polymeric Materials Using Schiff Base Functionalized Triazole Ligands, *Eur. J. Inorg. Chem.*, 2013, 803–812.

33 D. Savard, C. Cook, G. D. Enright, I. Korobkov, T. J. Burchell and M. Murugesu, Gradual spin crossover behaviour in a linear trinuclear Fe^{II} complex, *CrystEngComm*, 2011, **13**, 5190–5197.

34 O. G. Shakirova, L. G. Lavrenova, Y. G. Shvedenkov, G. A. Berezovskii, D. Y. Naumanov, L. A. Sheludyakova, G. V. Dolgushin and S. V. Larionov, Synthesis and Physicochemical Study of Iron(II), Cobalt(II), Nickel(II), and Copper(II) Complexes with 4-(2-Pyridyl)-1,2,4-Triazole, *Russ. J. Coord. Chem.*, 2004, **30**, 473–479.

35 Y. Garcia, P. Guionneau, G. Bravic, D. Chasseau, J. A. K. Howard, O. Kahn, V. Ksenofontov, S. Reiman and P. Gütlich, Synthesis, Crystal Structure, Magnetic Properties and ^{57}Fe Mössbauer Spectroscopy of the New Trinuclear [Fe3(4-(2′-hydroxyethyl)-1,2,4-triazole)6$(H_2O)_6$] $(CF_3SO_3)_6$ Spin Crossover Compound, *Eur. J. Inorg. Chem.*, 2000, 1531–1538.

36 J. J. A. Kolnaar, G. van Dijk, H. Kooijman, A. L. Spek, V. G. Ksenofontov, P. Gütlich, J. G. Haasnoot and J. Reedijk, Synthesis, Structure, Magnetic Behavior, and Mössbauer Spectroscopy of Two New Iron(II) Spin-Transition Compounds with the Ligand 4-Isopropyl-1,2,4-triazole. X-ray Structure of $[Fe_3$(4-isopropyl-1,2,4-triazole$)_6(H_2O)_6]$(tosylate$)_6\cdot 2H_2O$, *Inorg. Chem.*, 1997, **36**, 2433–2440.

37 M. Thomann, O. Kahn, J. Guilhem and F. Varret, Spin Conversion versus Antiferromagnetic Interaction in Iron(II) Trinuclear Species. Crystal Structures and Magnetic Properties of $[Fe_3(p\text{-}MeOptrz)_8(H_2O)_4](BF_4)_6$ and $[Fe_3(p\text{-}MeOprtz)_6(H_2O)_6](tos)_6$ [p-MeOptrz=4-(p-Methoxyphenyl)-1,2,4-triazole, tos = tosylate], *Inorg. Chem.*, 1994, **33**, 6029–6037.

38 G. Vos, R. A. Le Fêbre, R. A. G. de Graaff, J. G. Haasnoot and J. Reedijk, Unique high-spin-low-spin transition of the central ion in a linear, trinuclear iron(II) triazole compound, *J. Am. Chem. Soc.*, 1983, **105**, 1682–1683.

39 V. Gómez, C. S. de Pipaón, P. Maldonado-Illescas, J. C. Waerenborgh, E. Martin, J. Benet-Buchholz and J.-R. Galan-Máscarós, Easy Excited-State Trapping and Record High TTIESST in a Spin-Crossover Polyanionic Fe^{II} Trimer, *J. Am. Chem. Soc.*, 2015, **137**, 11924–11927.

40 V. Gómez, J. Benet-Buchholz, E. Martin and J.-R. Galan-Máscarós, Hysteretic Spin Crossover above Room Temperature and Magnetic Coupling in Trinuclear Transition-Metal Complexes with Anionic 1,2,4-Triazole Ligands, *Chem. – Eur. J.*, 2014, **20**, 5369–5379.

41 C. S. de Pipaón, P. Maldonado-Illescas, V. Gómez and J.-R. Galán-Mascarós, Spin Transition Kinetics in the Salt $[H_2N(CH_3)_2]_6[Fe_3(L)_6(H_2O)_6]$ (L=4-(1,2,4-triazol-4-yl)ethanedisulfonate), *Magnetochemistry*, 2016, **2**, 20.

42 S. Benmansour, C. Atmani, F. Setifi, S. Triki, M. Marchivie and C. J. Gómez-García, Polynitrile anions as ligands: From magnetic polymeric architectures to spin crossover materials, *Coord. Chem. Rev.*, 2010, **254**, 1468–1478.

43 E. Cuza, R. Motei, F. Setifi, A. Bentama, C. J. Gómez-García and S. Triki, Coordination isomerism in spin crossover (SCO) materials, *J. Appl. Phys.*, 2021, **129**, 145501.

44 S. Triki, F. Thétiot, F. Vandevelde, J. Sala-Pala and C. J. Gómez-García, New Magnetic Copper(II) Coordination Polymers with the Polynitrile Ligand (C[C(CN)2]3)2- and N-Donor Co-ligands, *Inorg. Chem.*, 2005, **44**, 4086–4093.

45 F. Thétiot, S. Triki, J. Sala-Pala and S. Golhen, Molecular assemblies based on tricyanomethanide units and copper (II) ions, *Inorg. Chim. Acta*, 2003, **350**, 314–320.

46 M. Decoster, J. E. Guerchais, Y. Le Mest, J. Sala-Pala, S. Triki and L. Toupet, Comparison of the properties of the 1,1,2,4,5,5-hexacyano-3-aza-penta-1,4-dienide [(NC)2C=C(CN)-NC(CN)=C(CN)2] unit as anion and as ligand. Crystal structures of $(Et_4N)C_{10}N_7$ and $[Ag(C_{10}N_7)]$, *Polyhedron*, 1996, **15**, 195–202.

47 N. Pittala, F. Thétiot, C. Charles, S. Triki, K. Boukheddaden, G. Chastanet and M. Marchivie, An unprecedented trinuclear Fe^{II} triazole-based complex exhibiting a concerted and complete sharp spin transition above room temperature, *Chem. Commun.*, 2017, **53**, 8356–8359.

48 M. Romanini, Y. Wang, K. Gürpinar, G. Ornelas, P. Lloveras, Y. Zhang, W. Zheng, M. Barrio, A. Aznar, A. Gràcia-Condal, B. Emre, O. Atakol, C. Popescu, H. Zhang, Y. Long, L. Balicas, J. L. Tamarit, A. Planes, M. Shatruk and L. Mañosa, Giant and Reversible Barocaloric Effect in Trinuclear Spin-Crossover Complex $Fe_3(bntrz)_6(tcnset)_6$, *Adv. Mater.*, 2021, 2008076.

49 H. O. Bayer, R. S. Cook and W. C. Von Mayer, Fungicidal use of a 1,2,4-triazole nickel salt complex, *US Patent*, 3821376A, 1974.

50 P. Guionneau, M. Marchivie, G. Bravic, J.-F. Létard and D. Chasseau, Structural Aspects of Spin Crossover. Example of the $[Fe^{II}Ln(NCS)2]$ Complexes, *Top. Curr. Chem.*, 2004, **234**, 97–128.

51 M. Buron-Le Cointe, J. Hébert, C. Baldé, N. Moisan, L. Toupet, P. Guionneau, J. F. Létard, E. Freysz, H. Cailleau and E. Collet, Intermolecular control of thermoswitching and photoswitching phenomena in two spin-crossover polymorphs, *Phys. Rev. B: Condens. Matter Mater. Phys.*, 2012, **85**, 064114.

52 J. K. McCusker, A. L. Rheingold and D. N. Hendrickson, Variable-Temperature Studies of Laser-Initiated $^5T_2 \rightarrow {}^1A_1$ Intersystem Crossing in Spin-Crossover Complexes: Empirical Correlations between Activation Parameters and

Ligand Structure in a Series of Polypyridyl Ferrous Complexes, *Inorg. Chem.*, 1996, **35**, 2100–2112.

53 M. Marchivie, P. Guionneau, J.-F. Létard and D. Chasseau, Photoinduced spin-transition: the role of the iron(II) environment distortion, *Acta Crystallogr., Sect. B: Struct. Sci.*, 2005, **61**, 25–28.

54 K. Boukheddaden, I. Shteto, B. Hôo and F. Varret, Dynamical model for spin-crossover solids. I. Relaxation effects in the mean-field approach, *Phys. Rev. B: Condens. Matter Mater. Phys.*, 2000, **62**, 14796–14805.

55 N. Ould-Moussa, G. Molnár, S. Bonhommeau, A. Zwick, S. Mouri, K. Tanaka, J. A. Real and A. Bousseksou, Selective Photoswitching of the Binuclear Spin Crossover Compound {[Fe(bt)$(NCS)_2$]$_2$(bpm)} into Two Distinct Macroscopic Phases, *Phys. Rev. Lett.*, 2005, **94**, 107205.

56 T. Matsumoto, G. N. Newton, T. Shiga, S. Hayami, Y. Matsui, H. Okamoto, R. Kumai, Y. Murakami and H. Oshio, Programmable spin-state switching in a mixed-valence spin-crossover iron grid, *Nat. Commun.*, 2014, **5**, 3865.

57 M. Arczyński, J. Stanek, B. Sieklucka, K. R. Dunbar and D. Pinkowicz, Site-Selective Photoswitching of Two Distinct Magnetic Chromophores in a Propeller-Like Molecule To Achieve Four Different Magnetic States, *J. Am. Chem. Soc.*, 2019, **141**, 19067–19077.

58 J.-F. Létard, Photomagnetism of iron(II) spin crossover complexes—the T(LIESST) approach, *J. Mater. Chem.*, 2006, **16**, 2550–2559.

59 A. Hauser, Light-Induced Spin Crossover and the High-Spin→Low-Spin Relaxation, in *Spin Crossover in Transition Metal Compounds II*, *Top Curr Chem*, Springer, Berlin, Heidelberg, 2004, vol. 234, pp. 155–198.

60 E. Milin, V. Patinec, S. Triki, E.-E. Bendeif, S. Pillet, M. Marchivie, G. Chastanet and K. Boukheddaden, Elastic Frustration Triggering Photoinduced Hidden Hysteresis and Multistability in a Two-Dimensional Photoswitchable Hofmann-Like Spin-Crossover Metal–Organic Framework, *Inorg. Chem.*, 2016, **55**, 11652–11661.

61 M. Mguenar Ndiaye, S. Pillet, E.-E. Bendeif, M. Marchivie, G. Chastanet, K. Boukheddaden and S. Triki, Hidden Hysteretic Behavior of a Paramagnetic Iron(II) Network Revealed by Light Irradiation, *Eur. J. Inorg. Chem.*, 2018, 305–313.

62 E. Cuza, C. D. Mekuimemba, N. Cosquer, F. Conan, S. Pillet, G. Chastanet and S. Triki, Spin Crossover and High-Spin State in Fe(II) Anionic Polymorphs Based on Tripodal Ligands, *Inorg. Chem.*, 2021, **60**, 6536–6549.

63 E. Cuza, S. Benmansour, N. Cosquer, F. Conan, S. Pillet, C. J. Gómez-García and S. Triki, Spin Cross-Over (SCO) Anionic Fe(II) Complexes Based on the Tripodal Ligand Tris (2-pyridyl)ethoxymethane, *Magnetochemistry*, 2020, **6**, 26.

64 Infrared and Raman Spectra of Inorganic and Coordination Compounds - Part B: Applications in Coordination, in *Organometallic, and Bioinorganic Chemistry*, ed. K. Nakamoto, Wiley, 2015.

65 M. Sorai and S. Seki, Phonon coupled cooperative low-spin $^1A_1$ high-spin $^5T_2$ transition in [Fe(phen)2(NCS)2] and [Fe$(phen)_2(NCSe)_2$] crystals, *J. Phys. Chem. Solids*, 1974, **35**, 555–570.

66 G. Brehm, M. Reiher, B. Le Guennic, M. Leibold, S. Schindler, F. W. Heinemann and S. Schneider, Investigation of the low-spin to high-spin transition in a novel [Fe(pmea)$(NCS)_2$] complex by IR and Raman spectroscopy and DFT calculations, *J. Raman Spectrosc.*, 2006, **37**, 108–122.

67 Y. Park, Y. M. Jung, S. Sarker, J.-J. Lee, Y. Lee, K. Lee, J. J. Oh and S.-W. Joo, Temperature-dependent infrared spectrum of $(Bu_4N)_2$[Ru(dcbpyH)$_2$-$(NCS)_2$] on nanocrystalline TiO2 surfaces, *Sol. Energy Mater. Sol. Cells*, 2010, **94**, 857–864.

68 V. Varma and J.-R. Fernandes, An infrared spectroscopic study of the low-spin-high-spin transition in $FexMn_{1-x}(Phen)_2(NCS)_2$: A composition-induced change in the order of the spin-state transition, *Chem. Phys. Lett.*, 1990, **167**, 367–370.

69 G. Sankar, J. M. Thomas, V. Varma, G. U. Kulkani and C. N. R. Rao, An investigation of the first-order spin-state transition in $Fe(Phen)_2(NCS)_2$ EXAFS and infrared spectroscopy, *Chem. Phys. Lett.*, 1996, **251**, 79–83.

70 E. Smit, D. de Waal and A. M. Heyns, The spin-transition complexes $[Fe(Htrz)_3](ClO_4)_2$ and $[Fe(NH_2trz)_3](ClO_4)_2$ I. FT-IR spectra of a low pressure and a low temperature phase transition, *Mater. Res. Bull.*, 2000, **35**, 1697–1707.

71 P. Durand, S. Pillet, E.-E. Bendeif, C. Carteret, M. Bouazaoui, H. El Hamzaoui, B. Capoen, L. Salmon, S. Hébert, J. Ghanbaja, L. Aranda and D. Schaniel, Room temperature bistability with wide thermal hysteresis in a spin crossover silica nanocomposite, *J. Mater. Chem. C*, 2013, **1**, 1933–1942.

72 M. Paez-Espejo, M. Sy and K. Boukheddaden, Elastic Frustration Causing Two-Step and Multistep Transitions in Spin-Crossover Solids: Emergence of Complex Antiferroelastic Structures, *J. Am. Chem. Soc.*, 2016, **138**, 3202–3210.